

RADIATION SIGNATURES OF SUB-LARMOR SCALE MAGNETIC FIELDS

MIKHAIL V. MEDVEDEV^{1,2,3}, JACOB TRIER FREDERIKSEN², TROELS HAUGBØLLE², ÅKE NORDLUND²

¹Institute for Advanced Study, School of Natural Sciences, Princeton, NJ 08540 and

²Niels Bohr International Academy, Blegdamsvej 17, DK-2199 København Ø, Denmark

Draft version May 25, 2022

ABSTRACT

Spontaneous rapid growth of strong magnetic fields is rather ubiquitous in high-energy density environments ranging from astrophysical sources (e.g., gamma-ray bursts and relativistic shocks), to reconnection, to laser-plasma interaction laboratory experiments, where they are produced by kinetic streaming instabilities of the Weibel type. Relativistic electrons propagating through these sub-Larmor-scale magnetic fields radiate in the jitter regime, in which the anisotropy of the magnetic fields and the particle distribution have a strong effect on the produced radiation. Here we develop the general theory of jitter radiation, which includes (i) anisotropic magnetic fields and electron velocity distributions, (ii) the effects of trapped electrons and (iii) extends the description to large deflection angles of radiating particles thus establishing a cross-over between the classical jitter and synchrotron regimes. Our results are in remarkable agreement with the radiation spectra obtained from particle-in-cell simulations of the classical Weibel instability. Particularly interesting is the onset of the field growth, when the transient hard synchrotron-violating spectra are common as a result of the dominant role of the trapped population. This effect can serve as a distinct observational signature of the violent field growth in astrophysical sources and lab experiments. It is also interesting that a system with small-scale fields tends to evolve toward the small-angle jitter regime, which can, under certain conditions, dominate the overall emission of a source.

Subject headings: radiation mechanisms — laboratory astrophysics — high-energy-density physics – gamma-ray bursts — shock waves — reconnection

arXiv:1003.0063v1 [astro-ph.HE] 27 Feb 2010

³ Also at: Department of Physics and Astronomy, University of Kansas, Lawrence, KS 66045 and Institute for Nuclear Fusion, RRC “Kurchatov Institute”, Moscow 123182, Russia

1. INTRODUCTION

There is a lore that a relativistic particle of charge e and a Lorentz factor γ moving through a magnetic field B produces synchrotron radiation, whose spectrum peaks at $\omega_s \sim (eB/mc)\gamma^2$, has an asymptotic $\omega^{1/3}$ dependence below the peak and falls off exponentially at higher frequencies (it makes a second power-law for an isotropic ensemble of particles having a power-law distribution in energy). This is often true, but not always. If the field is inhomogeneous on scales comparable or smaller than the particle Larmor radius, $\lambda_B \lesssim R_L \sim \gamma mc^2/e\langle B \rangle$, the produced radiation spectrum may be far different from synchrotron.

Gamma-ray bursts, supernovae shocks, relativistic pulsar winds and shocks, relativistic jets from quasars and active galactic nuclei, magnetic reconnection sites, plasmas produced by high-intensity lasers — they all are the high-energy density environments where conditions are favorable for the spontaneous magnetic field production. The field generation via the Weibel instability (Weibel 1959; Fried 1959; Silva, et al. 2003; Wiersma & Aichtenberg 2004) or its modifications (Dieckmann et al. 2006; Bret et al. 2008; Bret 2009; Frederiksen & Dieckmann 2008) has been predicted to occur in astrophysical shocks with low ambient magnetic field and rare particle collisions, e.g., in gamma-ray burst and large-scale structure shocks (Medvedev & Loeb 1999; Medvedev et al. 2006; Medvedev & Zakutnyaya 2009). It has been observed in numerical simulations of relativistic non-magnetized shocks (Nishikawa, et al. 2003; Frederiksen, et al. 2004; Spitkovsky 2008; Keshet et al. 2009; Nishikawa et al. 2009), nonrelativistic shocks unmagnetized and weakly magnetized shocks (Kato & Takabe 2008, 2010), cosmic rays interacting with a pre-shock medium (Niemiec et al. 2010), magnetic reconnection in electron-positron relativistic and non-relativistic plasmas (Zenitani & Hesse 2008; Swisdak et al. 2008; Liu et al. 2009), as well as in simulations of and even real laser plasma experiments (Ren et al. 2004; Tatarakis et al. 2003).

Given such a ubiquity of the process at hand, a natural question to ask is: Are there any observational signatures, which can benchmark the process in astrophysical sources and, if any, what can we learn about the physical conditions there? With the radiation techniques being developed and implemented into numerical codes (Heddal 2005; Nishikawa et al. 2008; Sironi & Spitkovsky 2009; Frederiksen, et al. 2010), we will soon be able to answer this question in detail (for instance, Medvedev & Spitkovsky 2009, showed that PIC simulations can realistically model some astrophysical sources). In order to correctly interpret the results of simulations and observational data, a comprehensive theory of radiation processes in a strong small-scale magnetic turbulence is, therefore, of great demand.

In this paper we develop a theory of jitter radiation that accounts for anisotropies of the magnetic field and particle velocity distributions, including a trapped population, and further extend the theory to the large angle jitter regime. Our theoretical findings are tested with dedicated particle-in-cell simulations. Interesting conclusions are presented in the final section.

2. THEORY

Radiation emitted from magnetic fields with small coherence length is *not* synchrotron, regardless of the actual shape of the produced spectrum. In some cases, the spectrum may resemble that of synchrotron, while in others it can be markedly different. What kind of spectrum is produced is, in general, set by how curved the particle paths are (i.e., how large their deflections from a straight line) compared to the relativistic beaming angle $\sim 1/\gamma$. In particular, when the deflection angle $\alpha \sim e\langle B \rangle \lambda_B / \gamma mc^2$ is smaller than the beaming angle the particle radiates in the classical jitter regime² (Medvedev 2000, 2006), in which the particle's velocity \mathbf{v} is almost constant, its path is almost straight, $\mathbf{r} = \mathbf{v}t$, and its acceleration $\mathbf{w} \equiv \dot{\mathbf{v}}$ is random and varies rapidly in time. Qualitatively, in the small-angle jitter regime, i.e., when the jitter parameter

$$\delta_{\text{jitter}} = e\langle B \rangle \lambda_B / mc^2 = \gamma \lambda_B / R_L \quad (1)$$

is small, $\delta_{\text{jitter}} \ll 1$, the spectrum has a peak at $\omega_j \sim (c/\lambda_B)\gamma^2$. The spectral shape is generally not universal at lower frequencies (it can be flat, $F_\nu \propto \nu^0$, in the isotropic magnetic turbulence but can also be as steep as $F_\nu \propto \nu^1$ in the presence of a strong anisotropy) and is usually a power-law above the peak, whose index is related to that of the spectrum of the magnetic turbulence and/or particle distribution.

2.1. Jitter radiation in the small deflection angle regime

Here we generalize the theory of classical jitter radiation (Medvedev 2000, 2006). Energy emitted by an accelerated relativistic particle and observed at infinity is given by the Poynting flux, which is easily calculated using Liénard-Wiechert (retarded) potentials. One arrives at the familiar expression (Landau & Lifshitz 1971) for the total energy emitted per unit solid angle $d\eta$ per unit frequency $d\omega$:

$$dW = \frac{e^2}{2\pi c^3} \frac{|\hat{\mathbf{n}} \times [(\hat{\mathbf{n}} - \hat{\mathbf{v}}\beta) \times \mathbf{w}_{\omega'}]|^2}{(1 - \beta \hat{\mathbf{v}} \cdot \hat{\mathbf{n}})^4} d\eta \frac{d\omega}{2\pi}, \quad (2)$$

where $\beta = v/c = (1 - \gamma^{-2})^{1/2}$, a “hat” denotes unit vectors, $\mathbf{w}_{\omega'} = \int \mathbf{w} e^{i\omega' t} dt$ is the Fourier component of the particle acceleration, the frequency in the comoving and observer's frames are related as $\omega' = \omega(1 - \beta \hat{\mathbf{v}} \cdot \hat{\mathbf{n}})$, and $\hat{\mathbf{n}}$ points toward the observer. Since acceleration in a magnetic field, $\mathbf{w} = (e/\gamma mc)\mathbf{v} \times \mathbf{B}$, is orthogonal to \mathbf{v} , the following holds:

$$|\hat{\mathbf{n}} \times [(\hat{\mathbf{n}} - \hat{\mathbf{v}}\beta) \times \mathbf{w}_{\omega'}]|^2 = |\mathbf{w}_{\omega'}|^2 (1 - \beta \hat{\mathbf{v}} \cdot \hat{\mathbf{n}})^2 - |\hat{\mathbf{n}} \cdot \mathbf{w}_{\omega'}|^2 \gamma^{-2}, \quad (3)$$

² A comprehensive analysis of jitter radiation in the large deflection angle regime requires a special study, but we provide semi-qualitative results below in Section 2.3. We should also note that contrary to the claims of (Fleishman 2006), none of their papers properly address the jitter regime. Approximations made in their analysis limit its applicability to the systems with large scale fields superimposed with small-scale perturbation which is homogeneous in k -space. None of these approximations hold for the Weibel-like magnetic turbulence, where there is no large scale field and the k -space representation of the small-scale fields is highly anisotropic.

where we keep the small term $\sim \gamma^{-2}$ because it can be important if a particle velocity distribution is structured at angular scales $\lesssim 1/\gamma$ and/or if γ is not very large.

So far, no approximations were made. Now we use the standard small-deflection approximation, $\mathbf{v} = \text{const}$, and we let the magnetic field vary, hence the Fourier image of acceleration and its projection onto $\hat{\mathbf{n}}$ are $w_{\omega'}^{\alpha} = (e\beta/\gamma m)^{\frac{1}{2}} e_{\alpha\beta\gamma}(\hat{\mathbf{v}}_{\beta} B_{\omega'}^{\gamma} - \hat{\mathbf{v}}_{\gamma} B_{\omega'}^{\beta})$ and $\hat{n}_{\alpha} w_{\omega'}^{\alpha} = (e\beta/\gamma m)^{\frac{1}{2}} e_{\alpha\beta\gamma} B_{\omega'}^{\alpha} (\hat{n}_{\beta} \hat{v}_{\gamma} - \hat{n}_{\gamma} \hat{v}_{\beta})$, where $e_{\alpha\beta\gamma}$ is the Levi-Civita tensor and in flat configuration space we do not distinguish between co- and contra-variant components. Now we immediately obtain³

$$|\mathbf{w}_{\omega'}|^2 = (\delta_{\alpha\beta} - \hat{v}_{\alpha} \hat{v}_{\beta}) W_{\omega'}^{\alpha\beta} \quad (4)$$

$$|\hat{\mathbf{n}} \cdot \mathbf{w}_{\omega'}|^2 = [\delta_{\alpha\beta} (1 - (\hat{\mathbf{v}} \cdot \hat{\mathbf{n}})^2) - \hat{v}_{\alpha} \hat{v}_{\beta} - \hat{n}_{\alpha} \hat{n}_{\beta} + (\hat{\mathbf{v}} \cdot \hat{\mathbf{n}})(\hat{v}_{\alpha} \hat{n}_{\beta} + \hat{v}_{\beta} \hat{n}_{\alpha})] W_{\omega'}^{\alpha\beta} \quad (5)$$

where $W_{\omega'}^{\alpha\beta} = (e\beta/\gamma m)^2 B_{\omega'}^{\alpha} B_{\omega'}^{*\beta}$ is the acceleration tensor, $B_{\omega'}$ represents the temporal variation of the field along the particle path and $\delta_{\alpha\beta}$ is the Kronecker symbol. In general, the field varies in space and time

$$\mathbf{B}(t, \mathbf{r}) = (2\pi)^{-4} \int e^{-i(\Omega t - \mathbf{k} \cdot \mathbf{r})} \mathbf{B}_{\Omega, \mathbf{k}} d\Omega d\mathbf{k}. \quad (6)$$

For a straight path $\mathbf{r} = \mathbf{r}_0 + \mathbf{v}t$, the field is a function of one independent variable t , hence

$$\begin{aligned} \mathbf{B}_{\omega'} &= (2\pi)^{-4} \int e^{i\omega t} dt (e^{-i(\Omega t - \mathbf{k} \cdot \mathbf{v}t - \mathbf{k} \cdot \mathbf{r}_0)} \mathbf{B}_{\Omega, \mathbf{k}}) d\Omega d\mathbf{k} \\ &= (2\pi)^{-3} \int \delta(\omega' - \Omega + \mathbf{k} \cdot \mathbf{v}) e^{i\mathbf{k} \cdot \mathbf{r}_0} \mathbf{B}_{\Omega, \mathbf{k}} d\Omega d\mathbf{k}, \end{aligned} \quad (7)$$

where we used the identity for the Dirac δ -function: $\int e^{i\xi t} dt = 2\pi \delta(\xi)$.

So far we dealt with a particular representation of a particle motion through magnetic turbulence. The assumption of ergodicity allows us to relate the ‘‘representative’’ history of B -field along a path to the spatial average over all possible initial positions \mathbf{r}_0 . This is a strong assumption, but it is valid for statistically homogeneous turbulence with no correlation between particles and fields (this is not strictly true for trapped particles, see below). Thus

$$\begin{aligned} \langle B_{\omega'}^{\alpha} B_{\omega'}^{*\beta} \rangle &= (2\pi)^{-6} V^{-1} \int B_{\Omega, \mathbf{k}}^{\alpha} B_{\Omega_1, \mathbf{k}_1}^{*\beta} \delta(\omega' - \Omega + \mathbf{k} \cdot \mathbf{v}) \delta(\omega' - \Omega_1 + \mathbf{k}_1 \cdot \mathbf{v}) e^{i(\mathbf{k} - \mathbf{k}_1) \cdot \mathbf{r}_0} d\mathbf{r}_0 d\Omega d\Omega_1 d\mathbf{k} d\mathbf{k}_1 \\ &= (2\pi)^{-3} V^{-1} \int B_{\Omega, \mathbf{k}}^{\alpha} B_{\Omega, \mathbf{k}}^{*\beta} \delta(\omega' - \Omega + \mathbf{k} \cdot \mathbf{v}) d\Omega d\mathbf{k}, \end{aligned} \quad (8)$$

where V is the volume occupied by the magnetic field and we again used the identity $\int e^{i(\mathbf{k} - \mathbf{k}_1) \cdot \mathbf{r}_0} d\mathbf{r}_0 = (2\pi)^3 \delta(\mathbf{k} - \mathbf{k}_1)$. It is trivial to prove via straightforward substitution⁴ that the spectral tensor $B_{\Omega, \mathbf{k}}^{\alpha} B_{\Omega, \mathbf{k}}^{*\beta}$ is just a Fourier image of the two-point autocorrelation tensor of the field, $\langle B_{\alpha} B_{\beta}(t, \mathbf{r}) \rangle \equiv T^{-1} V^{-1} \int B_{\alpha}(t', \mathbf{r}') B_{\beta}(t' - t, \mathbf{r}' - \mathbf{r}) dt' d\mathbf{r}'$, that is :

$$B_{\Omega, \mathbf{k}}^{\alpha} B_{\Omega, \mathbf{k}}^{*\beta} = TV \int \langle B_{\alpha} B_{\beta}(t, \mathbf{r}) \rangle e^{i(\Omega t - \mathbf{k} \cdot \mathbf{r})} dt d\mathbf{r}, \quad (9)$$

where T is the duration of an observation. Eqs. (2)–(5) and (8) completely determine the jitter radiation spectrum of a single particle in the small-deflection regime for an arbitrary field distribution.

When magnetic field is generated by a Weibel-type instability, particles bunch into localized streams – current filaments – thus determining a preferred direction, $\hat{\mathbf{s}}$, so that the magnetic field is predominantly in the plane orthogonal to $\hat{\mathbf{s}}$, as is illustrated in Figure 1, so

$$B_{\Omega, \mathbf{k}}^{\alpha} B_{\Omega, \mathbf{k}}^{*\beta} = |B_{\Omega, \mathbf{k}}|^2 (\delta_{\alpha\beta} - s_{\alpha} s_{\beta}), \quad (10)$$

where $|B_{\Omega, \mathbf{k}}|^2$ is the standard scalar spectrum of the field. The acceleration tensor becomes

$$W_{\omega'}^{\alpha\beta} = (\delta_{\alpha\beta} - s_{\alpha} s_{\beta}) |W_{\omega'}|^2, \quad (11)$$

where $|W_{\omega'}|^2$ is the scalar frequency spectrum of the particle acceleration. Finally, the spectral energy emitted by an ensemble of particles with a homogeneous anisotropic velocity distribution, $F(\mathbf{v})$, is

$$\begin{aligned} \frac{dW^{\text{ens}}}{d\eta d\omega} &= \frac{e^2}{(2\pi)^2 c^3} \int \left[\frac{1 + (\hat{\mathbf{s}} \cdot \hat{\mathbf{v}})^2}{(1 - \beta \hat{\mathbf{v}} \cdot \hat{\mathbf{n}})^2} - \frac{1}{\gamma^2} \frac{(\hat{\mathbf{s}} \cdot \hat{\mathbf{v}})^2 + (\hat{\mathbf{s}} \cdot \hat{\mathbf{n}})^2 - 2(\hat{\mathbf{v}} \cdot \hat{\mathbf{n}})(\hat{\mathbf{s}} \cdot \hat{\mathbf{v}})(\hat{\mathbf{s}} \cdot \hat{\mathbf{n}})}{(1 - \beta \hat{\mathbf{v}} \cdot \hat{\mathbf{n}})^4} \right] \\ &\quad \times \left[\left(\frac{e\beta}{\gamma m} \right)^2 \frac{1}{(2\pi)^3 V} \int |B_{\Omega, \mathbf{k}}|^2 \delta(\omega(1 - \beta \hat{\mathbf{v}} \cdot \hat{\mathbf{n}}) - \Omega + \mathbf{k} \cdot \mathbf{v}) d\Omega d\mathbf{k} \right] F(\mathbf{v}) d\mathbf{v}. \end{aligned} \quad (12)$$

³ Here we used the identities

$$e_{\alpha\beta\gamma} e_{\lambda\mu\nu} = \begin{vmatrix} \delta_{\alpha\lambda} & \delta_{\alpha\mu} & \delta_{\alpha\nu} \\ \delta_{\beta\lambda} & \delta_{\beta\mu} & \delta_{\beta\nu} \\ \delta_{\gamma\lambda} & \delta_{\gamma\mu} & \delta_{\gamma\nu} \end{vmatrix} \quad \text{and} \quad e_{\alpha\beta\gamma} e_{\alpha\mu\nu} = \begin{vmatrix} \delta_{\beta\mu} & \delta_{\beta\nu} \\ \delta_{\gamma\mu} & \delta_{\gamma\nu} \end{vmatrix}$$

⁴ Indeed, $B_{\Omega, \mathbf{k}}^{\alpha} B_{\Omega, \mathbf{k}}^{*\beta} = \int B_{\alpha}(t', \mathbf{r}') e^{i(\Omega t' - \mathbf{k} \cdot \mathbf{r}')} dt' d\mathbf{r}' \int B_{\beta}^*(t'', \mathbf{r}'') e^{-i(\Omega t'' - \mathbf{k} \cdot \mathbf{r}'')} dt'' d\mathbf{r}'' = \int [\int B_{\alpha}(t', \mathbf{r}') B_{\beta}(t' - t, \mathbf{r}' - \mathbf{r}) dt' d\mathbf{r}'] e^{i(\Omega t - \mathbf{k} \cdot \mathbf{r})} dt d\mathbf{r} = TV \int \langle B_{\alpha} B_{\beta}(t, \mathbf{r}) \rangle e^{i(\Omega t - \mathbf{k} \cdot \mathbf{r})} dt d\mathbf{r}$.

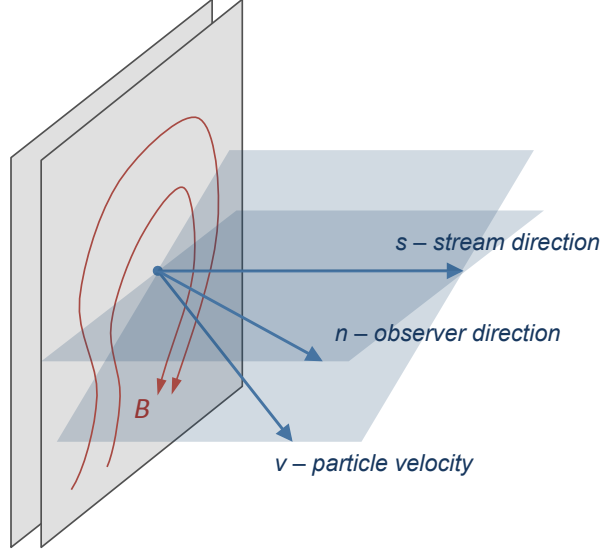


FIG. 1.— A cartoon showing the assumed planar distribution of the magnetic field typical of the Weibel turbulence and the triad of the unit vectors: \hat{s} , \hat{n} , \hat{v} .

The terms in this expression with septuple integration have clear physical meanings. The two terms in the first square brackets are the geometric factors coming from the product of $(\delta_{\alpha\beta} - s_{\alpha}s_{\beta})$ in Eq. (11) with the tensors in front of $W_{\omega'}^{\alpha\beta}$ in Eqs. (4), (5) respectively, the term in the second square brackets is simply the particle acceleration spectrum $|W_{\omega'}|^2$ and the outer integral weighted with the particle distribution function sums up the contributions of all particles in the system.

It is worthwhile to note that (i) the radiation spectrum of a single particle is proportional to the spectrum of the particle accelerations

$$dW/d\eta d\omega \propto |\mathbf{w}_{\omega'}|^2 \quad (13)$$

and, hence, is a ‘probe’ of the magnetic field structure along its path and (ii) the radiation is strongly beamed in the direction of the particle motion:

$$dW/d\eta \propto (1 - \beta(\hat{\mathbf{n}} \cdot \hat{\mathbf{v}}))^{-3} \propto (1 + (\gamma\vartheta)^2)^{-3}. \quad (14)$$

The latter expression is valid for $\gamma \gg 1$ and a small angle ϑ between \mathbf{v} and the line of sight. If the magnetic field is static ($\Omega = 0$) and its spatial spectrum has a peak at a characteristic coherence scale, $k_B \sim \lambda_B^{-1}$, then the single electron emissivity in the small angle regime is peaked at the frequency

$$\omega_{j,sm} \sim k_B c \gamma^2 \sim (c/\lambda_B) \gamma^2. \quad (15)$$

2.2. Jitter radiation from the trapped population

The Weibel instability (Weibel 1959) is driven by anisotropy of the particle distribution $F(\mathbf{v})$, which has been interpreted as the instability of streaming particles (Fried 1959). An infinitesimal transverse modulation of the stream density (i.e., the current density) results in transverse magnetic fields, which pinch the particles into filamentary structures and therefore enhance the initial perturbation. The filamentary distribution of particle streams is maintained by the self-generated magnetic fields. These stream particles are essentially trapped in the filaments for a long time and, hence, the ergodicity assumption used in the derivation of jitter radiation in Section 2.1 fails for them, so they are not accounted for by Eq. (12). These particles oscillate in filaments and radiate. Depending on the oscillation amplitude θ_m they emit radiation in the small-angle jitter regime if $\theta_m < 1/\gamma$ and in the large-angle jitter regime otherwise. However, in both cases one needs to know exact particle trajectories in order to calculate radiation. This is not possible for a generic magnetic field distribution. We illustrate this in the following simplified example of a two-dimensional straight filament.

If there is translational invariance along the filament, the parallel component of the generalized momentum of a particle is conserved: $P_{\parallel} = \gamma m v_{\parallel} - (e/c)A_{\parallel}(r_{\perp}) = \text{const}$, where $A_{\parallel}(r_{\perp})$ is the only non-zero component of the vector potential and it is a function of the transverse coordinate only. Since $\mathbf{E} = 0$ in the system, the particle energy is also conserved, therefore $v = \text{const}$. Because of the axial symmetry, the magnetic field is zero on the axis $r_{\perp} = 0$, so we can take $A_{\parallel}(0) = 0$. Then, it is straightforward to obtain the equation

$$\frac{dr_{\perp}}{dt} = \left[v^2 - \left(v_{\parallel}(0) + \frac{e}{\gamma m} A_{\parallel}(r_{\perp}) \right)^2 \right]^{1/2}, \quad (16)$$

which can be solved only in quadrature to obtain the particle trajectory as $t = t(r_{\perp})$; here $v_{\parallel}(0)$ is the parallel velocity on the axis of the filament. Even the turning points, $r_{\perp} = r_t$, can only be found implicitly: $v_{\parallel}(0) + (e/\gamma m)A_{\parallel}(r_t) = v$.

This model can be simplified further, as shown in Figure 2. For a uniform distribution of current near the filament axis, the magnetic field is a linear function of coordinates $B(r_{\perp}) = (r_{\perp}/r_0)B_0$, which holds for small displacements $r_{\perp} \ll r_0$, where r_0 is

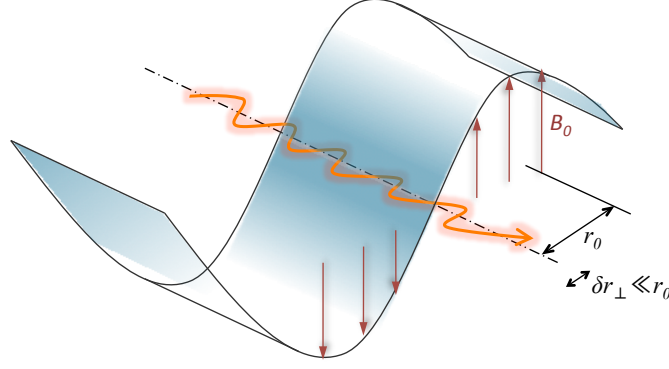


FIG. 2.— A cartoon showing a two-dimensional model of a radiating particle trapped in a filament with the magnetic field shown with vectors and the curved envelope. The color gradient illustrates the distribution of a current density. The δr_{\perp} is the particle oscillation amplitude, the filament size is r_0 and $B_0 = B(r_0)$.

the transverse size of a filament and B_0 is the field on its “surface”. The equation of motion $\dot{\mathbf{p}} = (e/c)\mathbf{v} \times \mathbf{B}$ for small amplitudes and $v \sim c$ reads:

$$\ddot{r}_{\perp} \simeq (eB_0/\gamma m)(r_{\perp}/r_0). \quad (17)$$

This is the equation of a harmonic oscillator. The streaming particles are trapped in filaments and oscillate with the characteristic bounce frequency

$$\Omega_b \simeq (eB_0/\gamma m r_0)^{1/2}. \quad (18)$$

Due to the oscillatory motion, the magnetic field in the frame comoving with the particle varies in time as $B(t) \simeq B_0 (r_t \sin(\Omega_b t)/r_0) \propto \sin(\Omega_b t)$. For small oscillation amplitudes⁵ $\theta_m \sim v_{\perp}/v \ll 1/\gamma$, the particle path can still be approximated as a straight line, so Eq. (12) can be used. To account for the bounce motion, the magnetic field spectrum can be approximately taken in the form⁶

$$|B_{\Omega, \mathbf{k}}|^2 \sim |B_{\mathbf{k}}|^2 \delta(\Omega - \Omega_b). \quad (19)$$

If there is a distribution of filaments of various sizes $r_{0,i}$ and strength $B_{0,i}$ in the system, the δ -function shall be substituted with the actual distribution of bounce frequencies, $f_b(\Omega)$. The observed radiation from the trapped population is peaked at the frequency

$$\omega_{j, \text{tr}} \sim \Omega_b \gamma^2. \quad (20)$$

2.3. Jitter radiation in the large deflection angle regime

When the deflection angle of a particle, $\theta_d \sim (\delta p)/p \sim p_{\perp}/p$, is greater than $1/\gamma$ (that is, $\delta_{\text{jitt}} > 1$), the radiation spectrum is determined by the geometry of the particle trajectory. The peak frequency depends on how fast the beaming cone sweeps through the line of sight, as in synchrotron radiation. The power of lower frequency harmonics, however, depends on the global structure of the path, such as the deflection angle θ_d or the oscillation amplitude θ_m of a trapped particle.

The radiation spectrum can be qualitatively obtained as follows. A generic particle trajectory can approximately be represented as a smoothly joined set of circular segments (arches) of a certain curvature (Larmor) radius, $R_L \sim \gamma m c^2/e(B)$, and an angular extent, θ_d , as is illustrated in Figure 3. Within each segment, $\theta < \theta_d$, the radiation harmonics are constructed coherently in the way similar to the standard synchrotron radiation. For a harmonics constructed over the angle θ , the radiation formation length is $l \sim R_L \theta$. Radiation emitted over this length is observed in the lab frame over the time interval $\Delta t \sim l/c\bar{\gamma}^2$, where $\bar{\gamma}$ is the mean Lorentz factor of the particle toward the observer, which is smaller than γ because the transverse motion of a particle is also relativistic: $\gamma_{\perp} \sim \gamma\theta$, hence $\bar{\gamma} \sim \gamma/\gamma_{\perp} \sim 1/\theta$. The observed frequency is $\omega_{\theta} \sim 1/\Delta t \sim \theta^3 c/R_L \sim (\gamma\theta)^{-3} \omega_0 \gamma^2$, where $\omega_0 = c/R_L$ is the fundamental (Larmor) frequency. The peak (synchrotron) frequency corresponds to the angle $\theta \sim 1/\gamma$ (i.e., when the observer is within the radiation cone) $\omega_{\text{synch}} = \omega_{1/\gamma} \sim \omega_0 \gamma^2$, hence $\omega_{\theta} \sim (\gamma\theta)^{-3} \omega_{\text{synch}}$. The radiation spectrum resembles synchrotron spectrum with $\omega^{1/3}$ law below the peak up to the break jitter frequency $\omega_j \sim \delta_{\text{jitt}}^{-3} \omega_{\text{synch}}$, where $\delta_{\text{jitt}} = (\gamma\theta_d)^{-1}$ by definition. At larger angular scales, $\theta > \theta_d$, the field is effectively incoherent, therefore radiation occurs in the small-angle jitter regime with the effective coherence scale $\lambda_B \sim R_L \theta_d$.

To summarize this subsection, the jitter radiation in the large angle regime corresponds to intermediate values of the jitter parameter: $1 < \delta_{\text{jitt}} < \gamma$. The radiation spectrum resembles the synchrotron spectrum, $\propto \omega^{1/3} \exp(-\omega/\omega_{\text{synch}})$, above the break frequency

$$\omega_{j, \text{br}} \sim \delta_{\text{jitt}}^{-3} \omega_{\text{synch}} \sim (\gamma \lambda_B / R_L)^{-3} (e(B)/mc) \gamma^2 \sim (c/\lambda_B)^3 (e(B)/\gamma mc)^{-2} \quad (21)$$

and is similar to the small angle jitter spectrum below this break. Although the small angle jitter spectrum is not universal, it is likely flat $\propto \omega^0$ because the field is generally more isotropic at larger scales and trapping of particles is less efficient, but spectra as hard as $\propto \omega^1$ cannot be excluded and may occur under certain conditions. Note that the break frequency, $\omega_{j, \text{br}}$

⁵ This is a more restrictive condition than $\delta r_{\perp} \ll r_0$, for which θ_m can also be larger than $1/\gamma$, depending on the value of r_0 .

⁶ Alternatively, one can set $\Omega = 0$ (static field) and modify the k_{\parallel} -spectrum of the magnetic field to have a sharp peak at $k_{\parallel} \sim k_b = \Omega_b/c$.

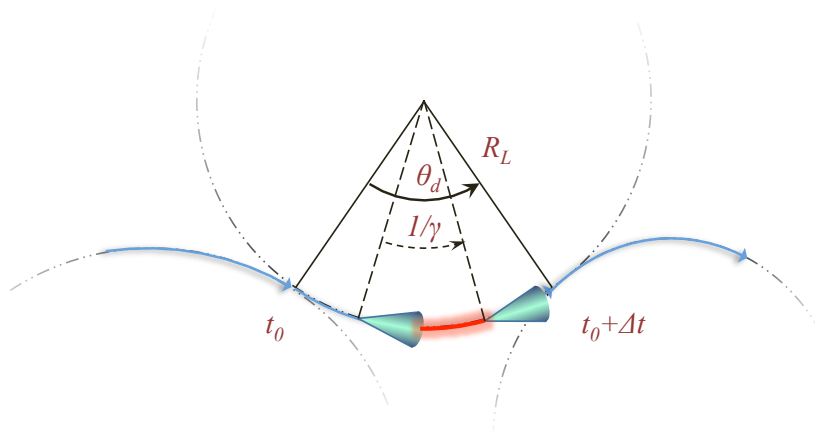


FIG. 3.— A cartoon showing the piecewise circular decomposition of a particle trajectory. For each segment of a certain curvature (Larmor) radius, R_L , and the deflection angle, θ_d , radiation is produced at times between t_0 and $t_0 + \Delta t$. Radiation is beamed directly toward an observer on the right within a highlighted $\sim 1/\gamma$ part of the segment.

depends on the product $\langle B \rangle \lambda_B$ via δ_{jitt} and the spectral peak ω_s measures B (they both proportional to γ^2 as well), so one can, in principle, determine the magnetic field correlation length λ_B from the spectrum alone. Finally, the case of $\delta_{\text{jitt}} > \gamma$ corresponds to synchrotron radiation.

3. COMPARISON WITH SPECTRA FROM PIC SIMULATIONS

3.1. PIC setup and results

The PIC simulations of the relativistic filamentation (Weibel) instability (Weibel 1959; Fried 1959) have been performed and radiation from the system has simultaneously been obtained. The simulations represent the classical Weibel instability with two equal density charge-neutral electron-positron and electron-ion plasma streams. Both two-dimensional and three dimensional setups with various initial bulk Lorentz factors, Γ , in the range of 2 to 15 were used. In three-dimensional electron-positron pair plasma simulations reported here (an exhaustive description is presented by Frederiksen, et al. 2010) the simulation box of 500^3 cells with periodic boundary conditions and with the resolution of 10 cells per the relativistic skin length, $\delta_e = \omega_{pe}/c = (4\pi e^2 n / \Gamma m_e c^2)^{1/2}$, was used. All physical spatial and temporal scales are expressed in units of the skin length and the plasma time, ω_{pe}^{-1} , respectively. Spectra are collected *in situ* during runtime using the PHOTONPLASMA code developed at the Niels Bohr Institute (Haugbølle 2005; Hededal 2005). In the simulations reported here, the total number of particles in the simulation box was $\sim 10^{10}$; however, the spectra were collected from about $N \sim 10^6$ particles and sub-cycling $\Delta t_{\text{rad}} \leq 10^{-1} \Delta t_{\text{PIC}}$ was used to resolve high radiation frequencies. The spectra were calculated coherently from the retarded electric fields of the ensemble of emitting particles

$$\frac{dW^{\text{ens}}}{d\omega d\eta} \propto \left| \int_{t_0}^{t_1} \sum_j^N E_{\text{ret},j} e^{i\omega\phi'} dt' \right|^2, \quad (22)$$

where the phase is $\phi' \equiv t' - \hat{\mathbf{n}} \cdot \mathbf{r}_0(t')/c$ and we neglected self-absorption, Rasin and other plasma effects. Thus, the obtained spectra represent ‘time-resolved’ radiation emitted within the time interval $\{t_0, t_1\}$. Snapshots of the system (particles, fields, radiation) are saved every two plasma times. Here we report the ‘head-on’ case, when the radiation is emitted along the initial streaming direction. The results for oblique and edge-on cases are reported elsewhere (Frederiksen, et al. 2010).

The PIC simulations cover the initial exponential growth of the magnetic field, saturation of the Weibel instability and the nonlinear evolution and mergers of current filaments (the merger model is developed in Medvedev, et al. 2005; Shvets et al. 2009) when the magnetic field gradually decays. These stages are seen in Figure 4, where

$$\epsilon_B = B^2 / [8\pi\Gamma(\Gamma - 1)nm_e c^2], \quad (23)$$

the magnetic field energy normalized by the total initial kinetic energy in the system, is plotted. The field strength reaches maximum $\sim 10\%$ at about saturation, $t \sim 10$. After saturation, the field strength decreases as $B(t) \propto t^{-1}$.

The particle distribution function, $F(\gamma_{v\perp}, \gamma_{v\parallel})$, and the transverse and parallel (with respect to the streaming direction) magnetic field spectra $|B_{k\perp}|^2 \equiv \langle B_{\perp}(k_{\perp})B_{\perp}^*(k_{\perp}) \rangle$ and $|B_{k\parallel}|^2 \equiv \langle B_{\perp}(k_{\parallel})B_{\perp}^*(k_{\parallel}) \rangle$ are shown in Figure 5 at representative times: during the linear stage of the instability with exponential growth ($t = 6$), at saturation ($t = 10$) and the late nonlinear regime ($t = 30$). Hereafter, we consider $\Gamma = 10$ case only; other cases with relativistic Γ are very similar.

The particle distribution is well described by a multi-Gaussian in $\gamma_{v_x}, \gamma_{v_y}, \gamma_{v_z}$. It is represented by two shifted Gaussians in the streaming (parallel) direction and a Gaussian in the perpendicular plane. The parallel and transverse temperatures are different and vary in time, so does the average (bulk) Lorentz factor of the interpenetrating streams.

Concerning the electromagnetic field, the electric fields and parallel magnetic fields are present but very weak (typically, less than a percent), so we only use \mathbf{B}_{\perp} in calculations of the field spectra. It was also found that the field spectrum is separable, that

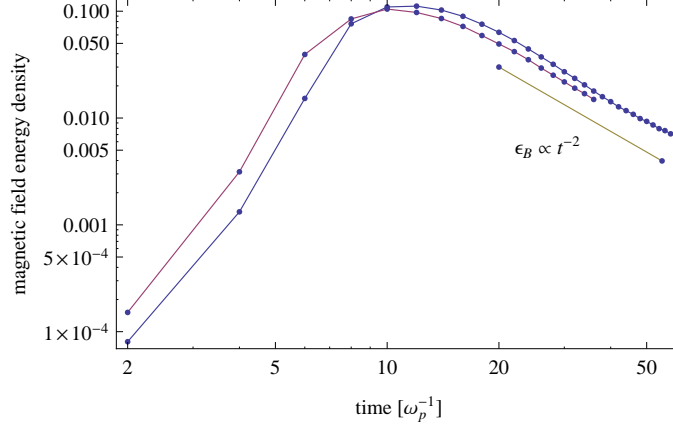


FIG. 4.— The magnetic field energy density normalized by the initial kinetic energy density of the streams, ϵ_B , versus time for two runs with $\Gamma = 2$ (blue) and $\Gamma = 10$ (red). At late times, $\epsilon_B \propto t^{-2}$.

is, it can be expressed as a product of two independent functions: $|B_{\mathbf{k}}|^2 = |B_{k_{\perp}}|^2 |B_{k_{\parallel}}|^2$, each being evaluated independently. In order to account for the entire evolution, we used a model of a Gaussian plus a smoothly broken power-law. Since the number of the fit parameters is rather large, some of them (but different) were kept fixed at various times. At early times, the perpendicular spectra, $|B_{k_{\perp}}|^2$, are fit well by a Gaussian or a double-power-law with a broad transition region whose width quickly reduces with time. At saturation, it is still a double-power-law. After saturation, the peak of the spectrum is much better described by a Gaussian component, which moves toward lower- k , leaving behind a single power-law at higher k . At late times, the power-law exhibits some curvature (downturn) at small k , where it intersects with the Gaussian component. In the beginning, the parallel spectra, $|B_{k_{\parallel}}|^2$, are flat (nearly at the noise level) with a broad peak at small k and then they develop a power-law. This peak is broad and is always at the largest scale (smallest k) corresponding to the box size. The peak is caused by the “causality horizon”: the filaments at distances greater than the light crossing time are uncorrelated thus producing white noise at small k . The peak width is decreasing as $\sim 1/t$, therefore. The bump at large k is likely due to the numerical Cherenkov instability. The power of these Fourier modes is very small and they do not significantly affect radiation spectra (although some signatures of it can be discerned). Overall, except for the linear phase of the instability, the temporal evolution of the parallel spectrum is very modest.

3.2. PIC and semi-analytic radiation spectra

Semi-analytical small-angle jitter spectra are obtained from Eq. (12) for each PIC snapshot using the available data for the particles $F(\mathbf{v}) = F(\gamma v_{\perp}, \gamma v_{\parallel})$ and fields $|B_{\mathbf{k}, \Omega}|^2 = f_{\perp}(k_{\perp}) f_{\parallel}(k_{\parallel}) f_b(\Omega)$, where $f_{\perp}(k_{\perp}) = |B_{k_{\perp}}|^2$, $f_{\parallel}(k_{\parallel}) = |B_{k_{\parallel}}|^2$ and the bounce frequency distribution is taken heuristically, using Eq. (18), as follows. If all the filaments are identical, then the total transverse size of the filament $\sim 2r_0$ corresponds to the peak of the $f_{\perp}(k_{\perp})$ distribution, $2r_0 \sim k_{\perp}^{-1}$. We conjecture that the profile of f_{\perp} , especially near the peak, describes the ensemble of filaments in the system. This is certainly violated at k_{\perp} greater than the skin scale beyond which no filaments exist. These scales are suppressed with an exponential factor in our model, therefore. Taking into account that $\Omega \sim c/r_0 \sim 2c/(2r_0) \sim 2k_{\perp}c$, we have $f_b(\Omega) = [2\Omega f_{\perp}(2\Omega) e^{-2\Omega/\omega_p} \Gamma(\Gamma-1)/\gamma^2]^{1/4}$. Although not rigorous, this prescription works well, likely because the main effect is due to the presence of a characteristic frequency Ω_b whereas the exact shape of $f_b(\Omega)$ is of lesser importance. We have also computed the synchrotron spectra for the same plasma parameters, i.e., the spectra one would expect from the large-scale magnetic field of the same strength with the same electron energy distribution. These spectra are similar to the large-angle jitter spectra, except for the low-frequency part, where a shallower spectrum is expected in the jitter regime (see discussion in Section 2.3).

The comparison of the PIC and semi-analytic spectra are shown in Fig. 6 for two time intervals: $t \in \{4, 12\}$ which corresponds to the early exponential growth before saturation and $t \in \{14, 26\}$ which corresponds to the late nonlinear phase of the filament merger and field decay. The predicted small-angle jitter and classical synchrotron spectra are plotted for comparison. The early-time PIC spectrum is in agreement with the semi-analytic prediction but not with the synchrotron spectrum both in the position of the peak and the overall spectral shape. In particular, (i) the PIC spectrum exhibits synchrotron-violating $\sim \omega^{0.5}$ scaling law below the peak with the subsequent flattening at lower frequencies, (ii) the high-frequency part in the PIC spectrum does not show the near-exponential roll-off (note that the electron distribution is still close to monoenergetic at this time), and (iii) the width of the peak region in the PIC is substantially narrower than it is in the synchrotron spectrum. The late-time PIC spectrum is generally consistent with synchrotron, except at frequencies below $\omega \sim 10$, where some flattening becomes evident.

The fact that the late-time PIC spectrum is synchrotron-like isn’t surprising because $\delta_{\text{jitt}} > 1$ in the run (see Section 2.3), which is evident from Figure 7, where we plotted the jitter parameter

$$\delta_{\text{jitt}} \simeq [2\epsilon_B \Gamma(\Gamma-1)]^{1/2} (k_{\text{skin}}/k_{\perp, \text{max}}), \quad (24)$$

where the peak of the $B_{k_{\perp}}$ -spectrum, $k_{\perp, \text{max}}$, is found numerically at each time and k_{skin} is the wave-number corresponding to the skin scale. What is more surprising is that the early-time PIC spectrum is not consistent with synchrotron at all. The explanation to this is simple. The particle distribution is highly anisotropic at these times: there are still well resolved particle streams which

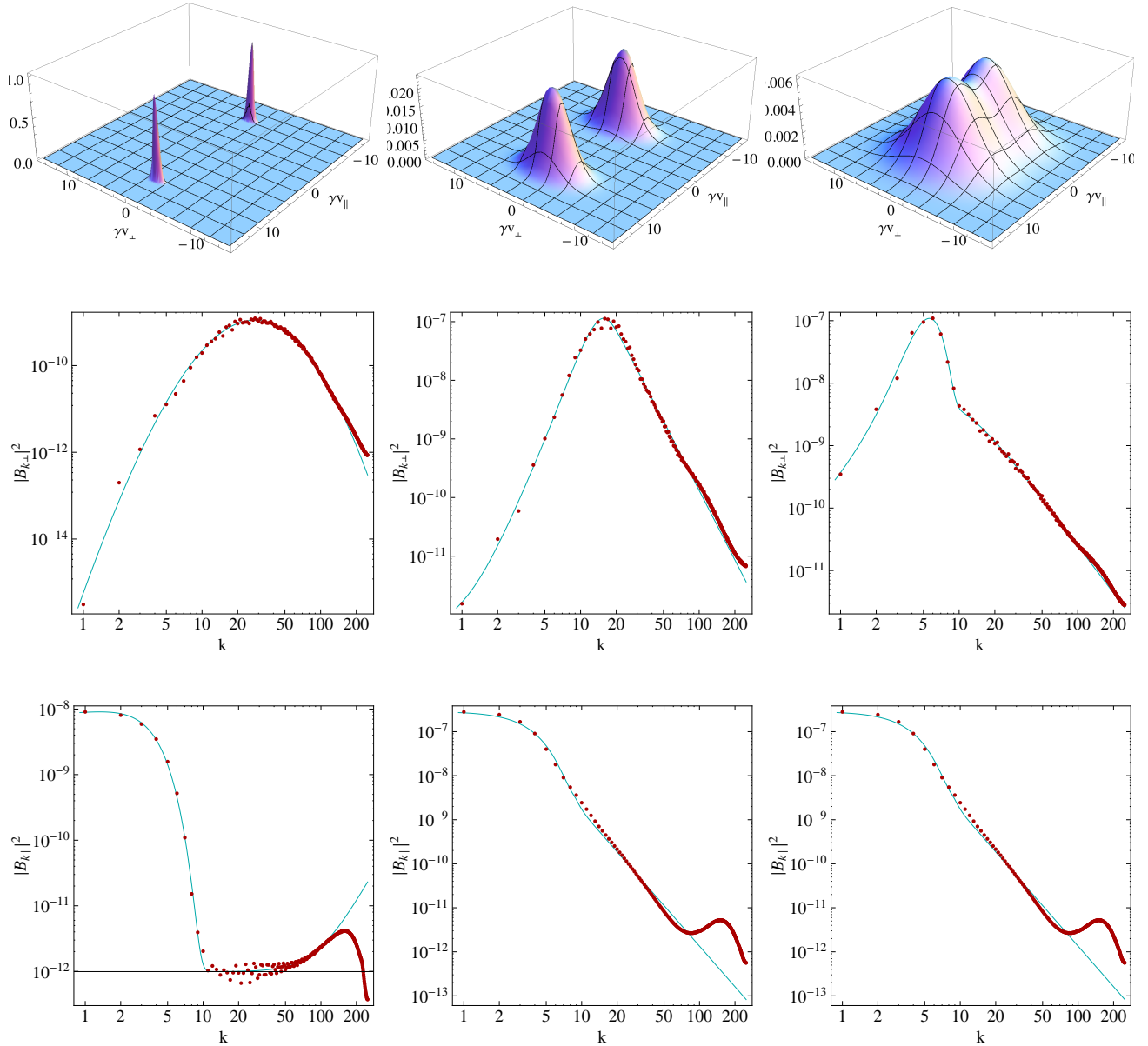


FIG. 5.— A representative sample of snapshots of (top to bottom) the particle distribution, $F(\gamma v_{\perp}, \gamma v_{\parallel})$, the perpendicular, $|B_{k\perp}|^2$, and parallel, $|B_{k\parallel}|^2$, magnetic field spectra before, at and after saturation (left to right: $t = 6, 10, 30$) for the 3D PIC simulation with $\Gamma = 10$. The blue curves are the empirical models, while the red dots are computed directly from the data.

form and are also trapped in the current filaments. For these particles, the size of the magnetic structures is irrelevant. As long as their angular deflections are small enough, they emit in the small-angle regime and produce hard spectra, no matter how large the δ_{jitt} parameter is. We have confirmed it by using tracer particles in a “frozen field” simulation. The full snapshot of particles and fields at $t = 8$ was used and in the subsequent simulation, the particles were allowed to move, but the fields were kept fixed (i.e., static and, of course, not self-consistent anymore). The evolution was traced over fourteen plasma times – long enough for the particles to become substantially isotropized, so that the number of trapped particles diminished drastically. The radiation spectrum obtained in this run is entirely consistent with the synchrotron spectrum from the particles with a thermal spread, as is evident from Figure 8.

4. CONCLUSIONS

The primary results of this paper are as follows. First, we present a general expression for the spectral energy per solid angle emitted by an ensemble of particles in the small-angle jitter approximation, Eq. (12). Second, we have found that the electrons streaming through the filaments and being trapped in them produce a transient hard spectrum, Eqs. (18,20). Third, we analyzed the large-angle deflection regime and showed that the spectrum starts to resemble the synchrotron spectrum near the peak, but a new spectral break at a lower frequency appears, Eq. (21). From the positions of the spectral peak and break, one can deduce the field correlation length.

Fourth, PIC simulations show that the radiation spectrum produced at the onset of and during the phase of the exponential

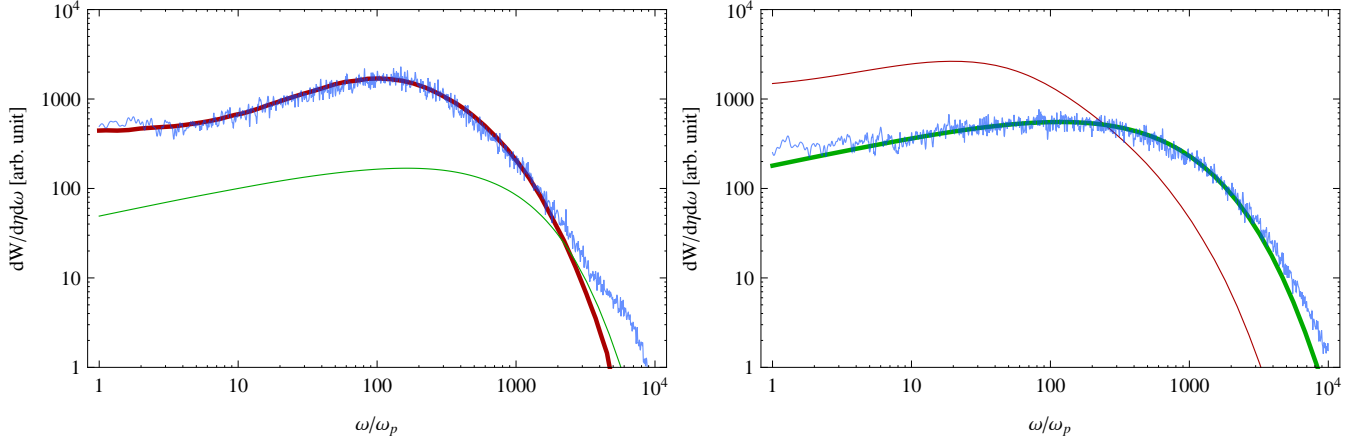


FIG. 6.— Radiation spectra at early, $t \in \{4, 12\}$, (left panel) and late, $t \in \{14, 26\}$, times (right panel). The spectra obtained ‘on-the-flight’ from 3D PIC $\Gamma = 10$ simulations of the Weibel instability in the e^+e^- -pair plasma are the two ‘noisy’ blue curves. The semi-analytic spectra from Eq. 12 are shown in red and the synchrotron spectra are in green. The early time PIC spectra are consistent with the hard (synchrotron violating) small-angle jitter emission and the late time emission is consistent with the large-angle jitter or synchrotron.

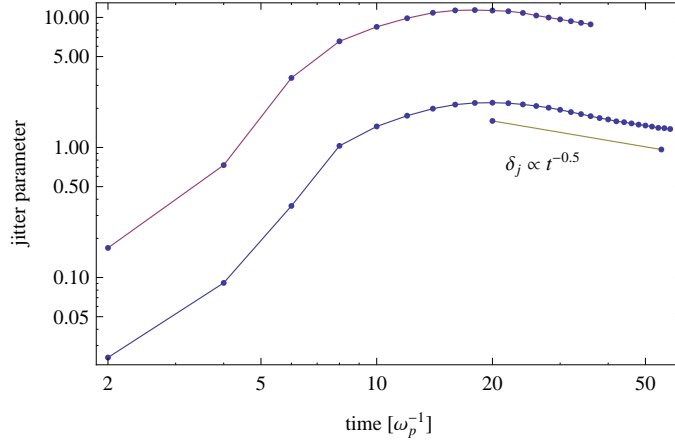


FIG. 7.— Jitter parameter as a function of time for two runs: $\Gamma = 10$ (top curve) and $\Gamma = 2$ (bottom curve). Asymptotically, $\delta_{\text{jitter}} \propto t^{-0.5}$.

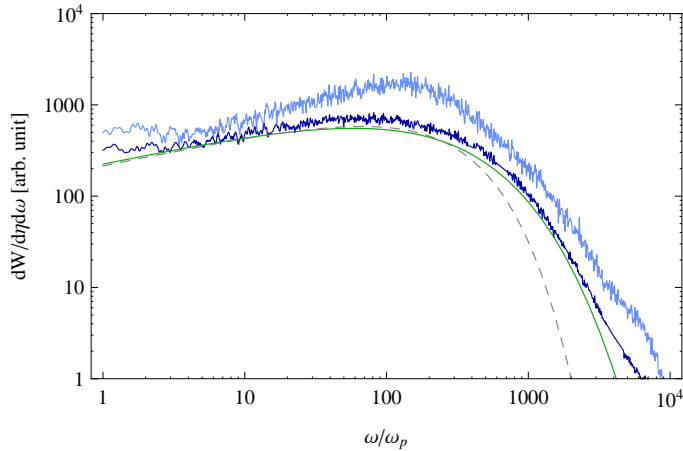


FIG. 8.— The PIC spectrum from the “frozen field” simulation (dark blue) and the original spectrum from Fig. 6(left) (light blue) are shown (in both, $\Gamma = 10$). The magnetic field structure is nearly identical in both, but the trapped population is practically absent in the “frozen-field” case. The corresponding synchrotron spectrum for the actual particle distribution (green) and for the monoenergetic electrons (dashed grey) are also shown for comparison.

growth of the magnetic field is grossly inconsistent with synchrotron, Fig. 6. The appearance of such a spectrum in the beginning of an emission episode can be used as a benchmark signal of the onset of the magnetic field generation in astrophysical sources

and laboratory experiments.

Fifth, although the spectra after saturation are consistent with the synchrotron ‘template’, an overall trend of the system toward the small-angle jitter regime (i.e., toward $\delta_{\text{jitt}} < 1$) is observed in Fig. 7, which suggest the scaling: $\delta_{\text{jitt}} \propto \sqrt{\epsilon_B} \Gamma(\omega_p t)^{-0.5}$. Although the magnetic field decays, it does so rather slowly, $B(t) \propto (\omega_p t)^{-1}$, see Fig. 4. So, if the field is continuously produced (as in the case of the propagating shock, for instance) the field decay can be compensated by the increase of the emitting volume, so that the total spectral emissivity will increase logarithmically, $P_{\text{tot}}(\omega) \propto \int B dV \propto \ln(\omega_p t)$, assuming these scalings hold at asymptotically late times. Since the plasma time $\sim \omega_p^{-1}$ is generally very short in astrophysical sources, the overall time-integrated (and even time resolved, but with a coarse temporal resolution) spectrum can be dominated by the small-angle jitter spectrum, which is expected to be flat (unless the strong anisotropy of the fields and/or particles is somehow maintained).

MVM work has been supported by NSF grant AST-0708213, NASA ATFP grant NNX-08AL39G and DOE grant DE-FG02-07ER54940. MVM also acknowledges support from The Ambrose Monell Foundation (IAS) and The Ib Henriksen Foundation (NBIA). Computer time was provided by the Danish Center for Scientific Computing (DCSC).

REFERENCES

- Bret, A. 2009, *ApJ*, 699, 990
 Bret, A., Gremillet, L., Bénisti, D., & Lefebvre, E. 2008, *Phys. Rev. Lett.*, 100, 205008
 Dieckmann, M. E., Frederiksen, J. T., Bret, A., & Shukla, P. K. 2006, *Phys. Plasmas*, 13, 112110
 Fleishman, G. D. 2006, *ApJ*, 638, 348
 Frederiksen, J. T., Hededal, C. B., Haugbølle, T., & Nordlund, Å. 2004, *ApJ*, 608, L13
 Frederiksen, J. T., & Dieckmann, M. E. 2008, *Phys. Plasmas*, 15, 094503
 Frederiksen, J. T., Haugbølle, T., Medvedev, M. V., & Nordlund, Å. 2010, in preparation
 Fried, B. D. 1959, *Phys. Fluids*, 2, 337
 Haugbølle, T. 2005, PhD thesis, Niels Bohr Institute [ArXiv:astro-ph/0510292]
 Hededal, C. 2005, PhD thesis, Niels Bohr Institute [ArXiv:astro-ph/0506559]
 Kato, T. N., & Takabe, H. 2008, *ApJ*, 681, L93
 Kato, T. N., & Takabe, H. 2010, *ApJ*, in press
 Keshet, U., Katz, B., Spitkovsky, A., & Waxman, E. 2009, *ApJ*, 693, L127
 Landau, L. D., & Lifshitz, E. M. 1971, *The classical theory of fields* (Oxford: Pergamon Press)
 Liu, Y.-H., Swisdak, M., & Drake, J. F. 2009, *Phys. Plasmas*, 16, 042101
 Medvedev, M. V., & Loeb, A. 1999, *ApJ*, 526, 697
 Medvedev, M. V. 2000, *ApJ*, 540, 704
 Medvedev, M. V., Fiore, M., Fonseca, R. A., Silva, L. O., Mori, W. B. 2005, *ApJ*, 618, L75
 Medvedev, M. V. 2006, *ApJ*, 637, 869
 Medvedev, M. V., Silva, L. O., & Kamionkowski, M. 2006, *ApJ*, 642, L1
 Medvedev, M. V., & Zakutnyaya, O. V. 2009, *ApJ*, 696, 2269
 Medvedev, M. V., & Spitkovsky, A. 2009, *ApJ*, 700, 956
 Niemiec, J., Pohl, M., Bret, A., & Stroman, T. 2010, *ApJ*, 709, 1148
 Nishikawa, K.-I., Hardee, P., Richardson, G., Preece, R., Sol, H., & Fishman, G. J. 2003, *ApJ*, 595, 555
 Nishikawa, K.-I., Mizuno, Y., Fishman, G. J., & Hardee, P. 2008, *International Journal of Modern Physics D*, 17, 1761
 Nishikawa, K.-I., Niemiec, J., Hardee, P. E., Medvedev, M. V., Sol, H.; Mizuno, Y.; Zhang, B., Pohl, M., Oka, M., Hartmann, D. H. 2009, *ApJ*, 698, L10
 Ren, C., Tzoufras, M., Tsung, F. S., Mori, W. B., Amorini, S., Fonseca, R. A., Silva, L. O., Adam, J. C., Heron, A. 2004, *Phys. Rev. Lett.*, 93, 185004
 Sironi, L., & Spitkovsky, A. 2009, *ApJ*, 707, L92
 Shvets, G., Polomarov, O., Khudik, V., Siemon, C., & Kaganovich, I. 2009, *Phys. Plasmas*, 16, 056303
 Spitkovsky, A. 2008, *ApJ*, 673, L39
 Silva, L. O., Fonseca, R. A., Tonge, J. W., Dawson, J. M., Mori, W. B., & Medvedev, M. V. 2003, *ApJ*, 596, L121
 Swisdak, M., Liu, Y.-H., & Drake, J.F. 2008, *ApJ*, 680, 999
 Tatarakis, M., Beg, F. N., Clark, E. L., Dangor, A. E., Edwards, R. D., Evans, R. G., Goldsack, T. J., Ledingham, K. W., Norreys, P. A., Sinclair, M. A., Wei, M.-S., Zepf, M., Krushelnick, K. 2003, *Phys. Rev. Lett.*, 90, 175001
 Weibel, E. S. 1959, *Phys. Rev. Lett.*, 2, 83
 Wiersma J., & Achtenberg, A. 2004, *A&A*, 428, 365
 Zenitani, S., & Hesse, M. 2008, *Physics of Plasmas*, 15, 022101